

Numerical analysis of ducted propeller and pumpjet propulsion system using periodic computational domain

Mehran Motallebi-Nejad¹ · Mohammad Bakhtiari¹ · Hassan Ghassemi¹ · Manouchehr Fadavie¹

Received: 16 March 2016 / Accepted: 24 February 2017 / Published online: 15 March 2017
© JASNAOE 2017

Abstract Nowadays surface and underwater vessels with modern propulsion systems and proper hydro-acoustic performance have been emerged. Pumpjet is one of these new systems, mainly employed for the underwater applications. The advantage of pumpjet over other propulsion systems can be defined by two factors including high efficiency and very low acoustic effects. In this study, the finite volume method (FVM) is implemented to predict hydrodynamic forces acting on a pumpjet propulsion system using ANSYS-CFX solver. The RANS equations with SST $k-\omega$ turbulent model are solved in a periodic computational domain around the pumpjet. First, the presented numerical model is applied to a ducted propeller and the numerical results obtained for thrust and torque coefficients and hydrodynamic efficiency are presented and compared with available experimental results. Then, this model is used for analysis of flow around the pumpjet. The numerical results of thrust, torque and hydrodynamic efficiency for pumpjet are presented in different advance coefficients. Velocity and pressure distributions on pumpjet blades are also shown and discussed.

Keywords Pumpjet · Finite volume method · Thrust · Torque · Efficiency

1 Introduction

Pumpjet propulsion system includes rotor (a moving part), stator (a stationary part) and a duct covering rotor and stator, as illustrated in Fig. 1. The task of stator is to convert the outlet rotational flow of the rotor to an axial flow and prevent the energy loss. The duct controls the flow of water entering the system and makes it more uniform and also acts as a limiting factor for sound propagation. It should be noted that the duct implemented in pumpjet is a decelerating duct [1]. Figure 2 shows a sample of the application of Pumpjet for an offshore vessel [2].

Generally, pumpjets are systems that produce high propulsive efficiency using retarded wake flow. In the conventional propeller, the velocity of flow coming into a propeller blade is approximately equal to the vehicle speed, since the propeller diameter is large enough to use the free stream velocity. In order for the propeller to generate any effective thrust, it should accelerate the flow, the outflow velocity being faster than the inflow velocity. It means that certain amount of the energy inducted to the fluid by the thruster is lost in the surrounding water. On the other hand, the pumpjet receives the retarded flow velocity, slower than the free stream velocity. To generate a thrust, again this flow should be accelerated. However, if the pumpjet is properly designed, the accelerated flow velocity can nearly be that of the vehicle speed. If one looks from the inertial frame, the ejected flow out of the pumpjet has almost no absolute velocity and thus leaves hardly any jet wake after the vehicle passed. There exists much less wasted energy in the flow field after a vehicle with a pumpjet passes. This is the major reason why the pumpjet can produce such high propulsive efficiency such as 90% or higher if it is properly designed. In contrast, one of the problems in analysis of the pumpjet is about the velocity-retarded wake flow. Velocity

✉ Hassan Ghassemi
gasemi@aut.ac.ir

¹ Department of Maritime Engineering, Amirkabir University of Technology, 424 Hafez Ave, Tehran 15875-4413, Iran

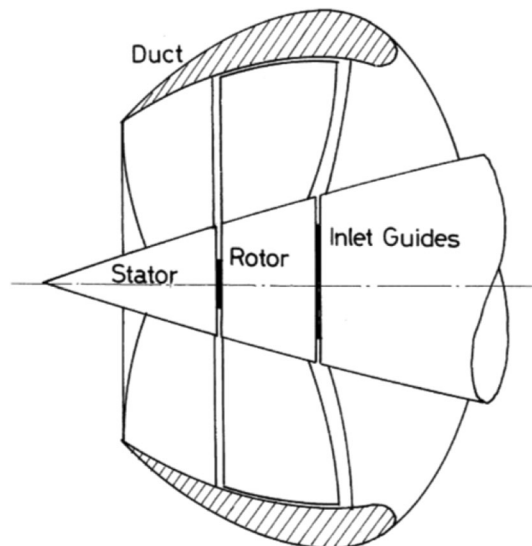


Fig. 1 Schematic of the pumpjet propulsion system

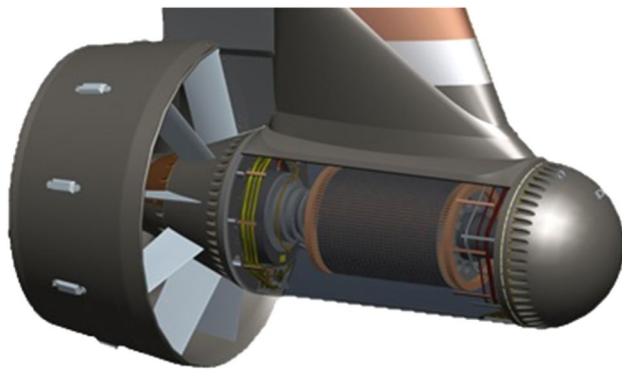


Fig. 2 Application of pumpjet for an offshore vessel

changes in the radial direction are very high as the velocity at the hub is only 30% of the free stream velocity and rapidly increases to 75% at the duct internal boundary. This variation caused by the viscous boundary layer leads to crucial problems in design and obtaining high efficiency [3].

Until now, many studies have been performed on pumpjet propulsion systems. Henderson et al. introduced a method for design of pumpjet in 1964 [4]. Furuya and Chiang, in 1988, presented a report entitled “A New Pumpjet Design Theory”, describing the blade-to-blade design approach and related issues [3]. In 1993, Zierke et al. presented experimental results of an axial-flow pump with a row of fixed blades at high Reynolds number, which helps to understand the physics of complex flow fields for pumps and also provide the information needed for numerical analysis [5]. Hayden studied the impact of rotor suction on rotor–stator interaction noise in 1994 [6]. Lee et al. analyzed an axial-flow pump by RANS method and compared

the numerical results with Zierke’s experimental results [7]. In 2001, Ivanell modeled a torpedo with pumpjet propulsion system numerically and compared his results with experimental test for his Master thesis [8]. In 2005, Park et al. investigated an axial flow pump with fixed blades by RANS approach and compared their results with Zeirek’s [9]. Numerical analysis of fluid flow on a high speed underwater vehicle with pumpjet propulsion system was studied by Das et al. in 2006 [10]. Suryanarayana et al., in three different papers, investigated resistance and thrust forces of an underwater vehicle with a pumpjet propulsion system, specified the diagrams of hydrodynamic coefficients and predicted cavitation of pumpjet by experimental test in 2010 [11–13]. A numerical analysis of rotor–stator interaction to predict the propeller and rudder behavior was presented by He for his PhD thesis [14]. In 2012, Duan et al. studied the flow around the underwater vehicle with pumpjet propulsion system using Fluent software and k- ϵ RNG turbulent model [15]. Rao et al. also investigated the unsteady interactions of a ducted propeller with stator blades before the propeller in 2013 [16]. Xiao Jun et al. studied the hydrodynamic coefficients of a distributed pumpjet propulsion system for underwater vehicle by numerical method in 2014 [17]. Ahn and Kwon analyzed a pumpjet with and without a ring around the propeller via numerical analysis in 2015 [18]. In the same year, Huyer studied the lateral forces of stator for control of an underwater vehicle by numerical method [19]. Performance analysis of the decelerating ducted propeller carried out by Bontempo et al. in 2015 [20]. In the same year, Marko and Roko developed a neural network prediction model to estimate the open water characteristics of the four blade Ka series propeller in combination with the 19 A accelerating nozzle [21]. Sun et al. investigated the hydrodynamic performance of propeller boss cap fins in a propeller-rudder system in 2016; their numerical simulation was based on the Navier–Stokes equations solved with a sliding mesh and the SST (Shear Stress Transport) k- ω turbulence model [22]. The open water performance of the Ka-series propellers at various pitch and expanded area ratios in combination with the 19 A duct by employing the panel method and the RANSE code ANSYS-CFX investigated by Yu et al. [23]. The cavitation performance and tip clearance cavitation were studied for the pumpjet propulsor on a UUV based on URANS by Pana et al. in 2016 [24].

Generally, the numerical studies for the pumpjet are scarce. This paper is presented to analyze the hydrodynamic characteristics of the pumpjet. Regarding this objective, the transient flow around a pumpjet is investigated using a commercial CFD solver. The RANS equations with SST k- ω turbulent model are solved in a periodic computational domain around the pumpjet by ANSYS-CFX code. Due to the lack of experimental data for the pumpjet model under investigation,

first the presented numerical model is applied to a ducted propeller model as a simplified model of the pumpjet (a pumpjet is a ducted propeller with fixed blades located after the propeller). For this purpose, a ducted propeller (Kaplan K4-70 with 19 A duct) is selected. The experimental results of this model are available [25].

The paper sections are organized as follows. Section 2 describes the governing equations. In Sect. 3, the presented numerical model including governing equations, solution domain, boundary conditions and computational grid are applied to the ducted propeller and verification and validation study for numerical results is provided. The numerical modeling of pumpjet is presented and discussed in Sect. 4, and finally conclusions are given in Sect. 5.

2 Governing equations

It is assumed that fluid is incompressible. The governing equations are the mass and momentum conservations. Using the Reynolds averaging approach, the Navier–Stokes equation can be stated as:

$$\frac{\partial u_i}{\partial x_i} = 0 \tag{1}$$

$$\frac{\partial}{\partial t}(\rho u_i) + \frac{\partial}{\partial x_j}(\rho u_i u_j) = -\frac{\partial p}{\partial x_i} + \frac{\partial}{\partial x_j} \left[\mu \frac{\partial u_i}{\partial x_j} - \overline{\rho u'_i u'_j} \right] + f_i \tag{2}$$

where $-\overline{\rho u'_i u'_j}$ represents Reynolds stresses.

Reynolds stresses in Eq. 2 are modeled using Boussinesq hypothesis that relates the Reynolds stresses to the mean velocity gradients as follows:

$$-\overline{\rho u'_i u'_j} = \mu_t \left(\frac{\partial u_i}{\partial x_j} + \frac{\partial u_j}{\partial x_i} \right) - \frac{2}{3} \left(\rho k + \mu_t \frac{\partial u_k}{\partial x_k} \right) \delta_{ij} \tag{3}$$

In this study, the two-equation Shear-Stress Transport (SST) k - ω turbulence model is used for modeling turbulent viscosity. The turbulence kinetic energy, k , and the specific dissipation rate, ω , are obtained from the following transport equations:

$$\frac{\partial}{\partial t}(\rho k) + \frac{\partial}{\partial x_i}(\rho k u_i) = \frac{\partial}{\partial x_j} \left[\left(\mu + \frac{\mu_t}{\sigma_k} \right) \frac{\partial k}{\partial x_j} \right] + G_k - \rho \beta^* k \omega \tag{4}$$

$$\frac{\partial}{\partial t}(\rho \omega) + \frac{\partial}{\partial x_j}(\rho \omega u_j) = \frac{\partial}{\partial x_j} \left[\left(\mu + \frac{\mu_t}{\sigma_\omega} \right) \frac{\partial \omega}{\partial x_j} \right] + G_\omega - \rho \beta \omega^2 + D_\omega \tag{5}$$

where \tilde{G}_k and G_ω are generation of k and ω , respectively. σ_k and σ_ω are the turbulent Prandtl numbers for k and ω :

$$\sigma_k = \frac{1}{F_1/\sigma_{k,1} + (1 - F_1)/\sigma_{k,2}} \tag{6}$$

$$\sigma_\omega = \frac{1}{F_1/\sigma_{\omega,1} + (1 - F_1)/\sigma_{\omega,2}} \tag{7}$$

where F_1 and F_2 are blending functions.

The turbulent viscosity, μ_t , is computed as follows:

$$\mu_t = \frac{\rho k}{\omega} \frac{1}{\max \left[\frac{1}{\alpha^*}, \frac{S F_2}{\alpha_1 \omega} \right]} \tag{8}$$

Coefficient α^* damps the turbulent viscosity causing a low-Reynolds-number correction.

2.1 Hydrodynamic coefficients

When a propeller (or rotor) with diameter (D) is rotating with angular velocity ω ($= 2\pi n$) and advance velocity (V_A), it generates thrust and torque. The hydrodynamic performance characteristics of the propeller can be defined as the non-dimensional coefficients such as the advance coefficient (J), the propeller thrust coefficient (K_t), the propeller torque coefficient (K_q) and efficiency (η) which can be computed respectively as follows [1]:

$$J = \frac{V_A}{nD}, \quad K_{t\text{prop}} = \frac{T_{\text{prop}}}{\rho n^2 D^4}, \quad K_{t\text{in}} = \frac{T_n}{\rho n^2 D^4} \tag{9}$$

$$K_q = \frac{Q}{\rho n^2 D^5}, \quad \eta = \frac{(K_t + K_{t\text{in}})}{K_q} \cdot \frac{J}{2\pi}$$

where T_{prop} and Q are thrust and torque of the propeller, respectively. T_n is thrust of the duct. It should be mentioned that the duct (nozzle) produces thrust only while propeller generates thrust and torque. Also, for the pumpjet similar formulae are defined.

3 Numerical analysis of a ducted propeller

In this section, the presented numerical model is applied to a ducted propeller with available experimental results. For this purpose, a 4-blades Kaplan series propeller with expanded area ratio of 0.7, pitch ratio of 1 and diameter of 30 cm with a 19 A duct is selected [22], as a simplified model of the pumpjet. The three-dimensional model of the ducted propeller is shown in Fig. 3.

3.1 Solution domain and boundary conditions

According to the geometry of the ducted propeller, a cylinder is used to determine the solution domain of fluid flow. The distances of outer boundaries from the ducted propeller are considered large enough to apply the actual boundary conditions. Accordingly, the inlet flow boundary is set at a distance of $4D$ from duct in upstream flow, the outlet boundary is set at a distance of $6D$ from duct in

downstream flow and the diameter of the lateral cylindrical boundary is considered $3D$, where D is propeller diameter. The dimensions of solution domain are shown in Fig. 4.

Given that the flow around the propeller can be considered steady in a Moving Reference Frame (MRF) rotating with an angular velocity equal to propeller velocity; here the Moving Reference Frame method is used for the whole solution domain. In this case, only the additional acceleration terms are appeared in the governing equations. The applied boundary conditions in stationary or moving reference frame are shown in Table 1.

3.2 Computational grid

The most important step in a numerical modeling is computational grid generation. The type and size of the grid

cells has a significant impact on the accuracy and convergence of the solution. Due to the complexity of propeller geometry, an unstructured mesh including tetrahedral cells is used here for domain discretization (Fig. 5a). To better capture the surface curvatures, the size of cells on propeller surface is considered adequately fine (Fig. 5b). Also, in a cylindrical fluid zone near the ducted propeller, the size of cells is reduced. In addition, due to the high velocity gradients in the direction normal to the walls inside the boundary layer flow, an inflation layer mesh is applied to these regions (Fig. 5c). In generation of an inflation layer mesh, the distance of the first computational node from the wall (thickness of the first layer) and the number of layers inside the boundary layer flow are very important and depend heavily on turbulent flow model selected. In this study, low Reynolds number SST turbulent model is implemented. For

Fig. 3 Three-dimensional model of the ducted propeller

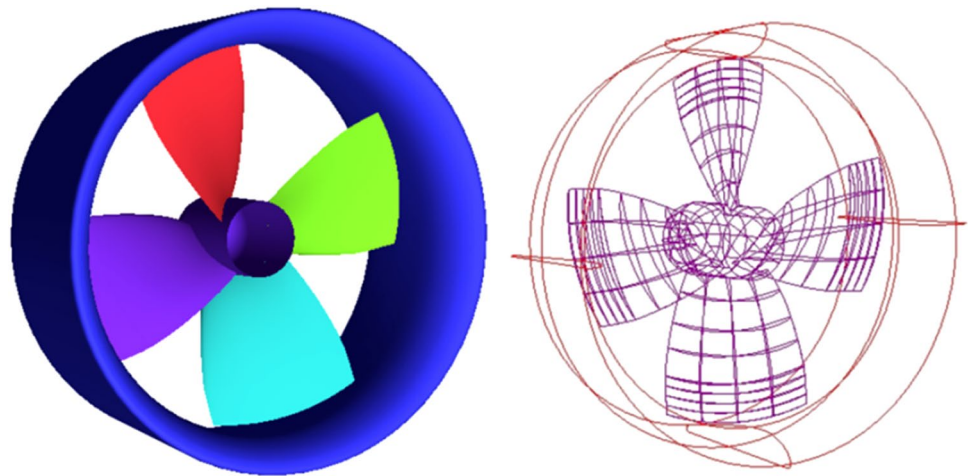


Fig. 4 Dimensions of solution domain

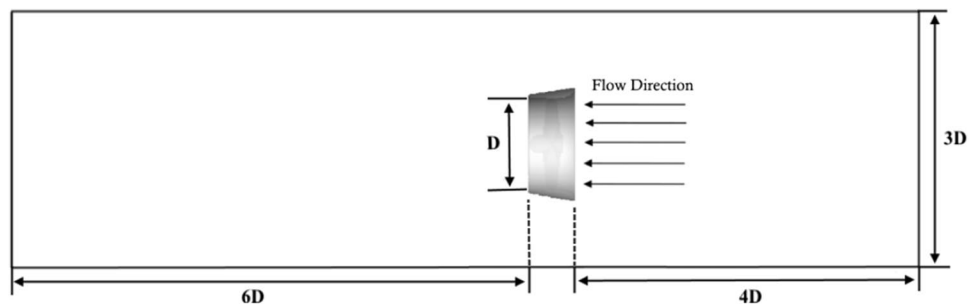
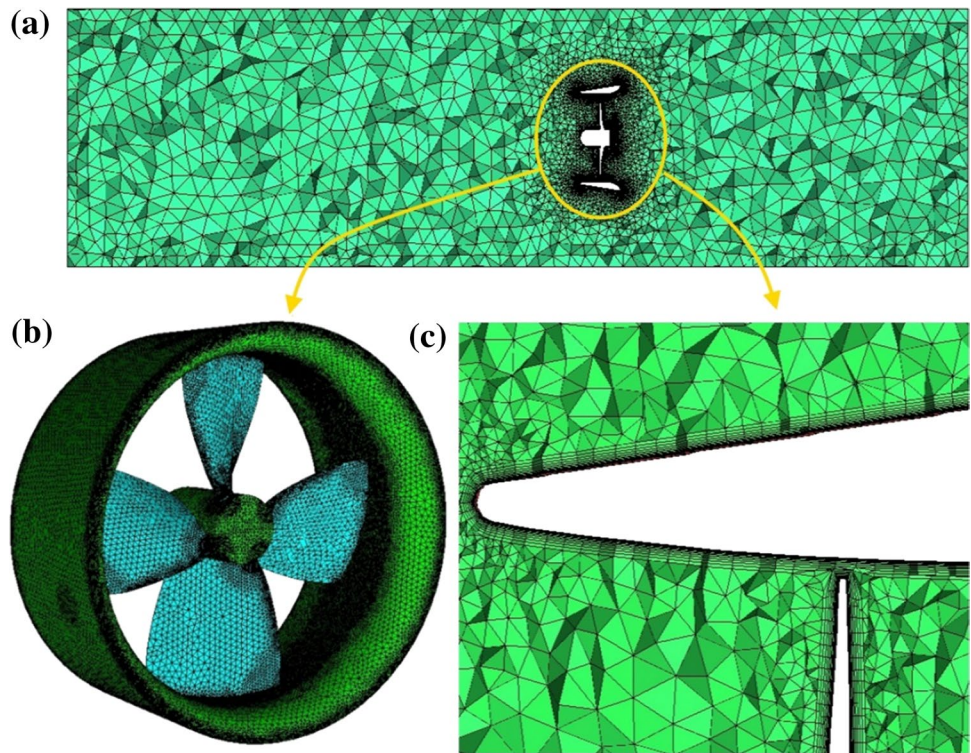


Table 1 Applied boundary conditions

Boundary	Type of boundary condition	Explanation
Inlet	Velocity inlet	Calculated from the propeller advance coefficient
Outlet	Pressure outlet	The static pressure is set relative to the reference pressure
Lateral border	Free slip wall	Velocity is considered zero relative to the stationary reference frame
Propeller and hub surface	No slip wall	Velocity is considered zero relative to the moving reference frame
Duct	No slip wall	Velocity is considered zero relative to the stationary reference frame

Fig. 5 **a** Computational grid around the ducted propeller, **b** surface mesh on propeller and duct, **c** boundary layer mesh on duct and propeller tip

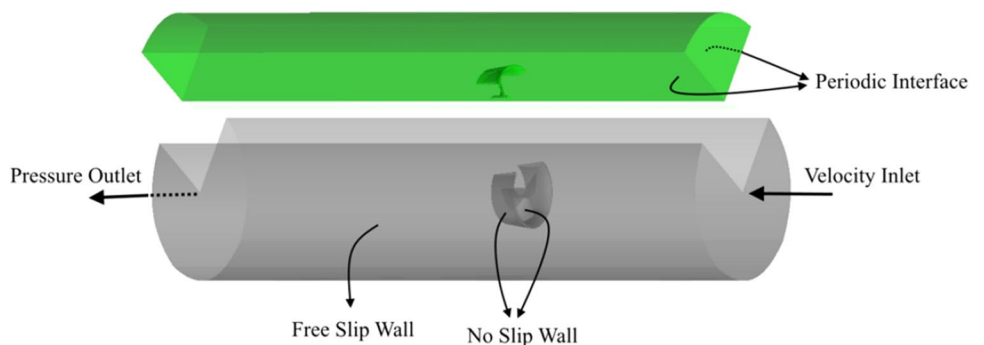


the finest computational grid, the non-dimensional thickness of the first inflation layer on the wall is considered to be $y^+ = 1$ and the number of the inflation layers inside the boundary layer flow is about 20. The number of cells in the coarsest computational grid is 3,863,631. Studying the grid convergence will be required to finer grids with large number of cells. Due to the limitations in computational resources, the flow around the propeller is assumed periodic and subsequently, the computational domain is reduced to a single blade. As a result, here calculations are conducted in only a quarter of the total domain. The number of cells in periodic domain for the coarsest computational grid is 930,102, which is approximately a quarter of the number of cells in complete domain with the same cell size. A schematic of periodic domain isolated from the complete domain is shown in Fig. 6. The boundary

conditions are also presented in the same figure. To verify the accuracy of the periodic assumption, a comparison between the results of complete domain, periodic domain and experimental results for an advance coefficient of 0.6 are introduced in Table 3. The applied boundary conditions for periodic domain are similar to complete domain and just one boundary condition is added for the interface boundary.

To estimate the discretization error and numerical uncertainty, a grid convergence study was done based on the Grid Convergence Method (GCI) described in [26]. The procedure proposed by [26] is an acceptable and a recommended method that have been evaluated over several 100 CFD cases. For this purpose, calculations were performed for three different grid resolutions in periodic domain. The total number of cells in different grids is $N_1=1,911,436$,

Fig. 6 Schematic of the periodic domain isolated from the complete domain, and applied boundary conditions



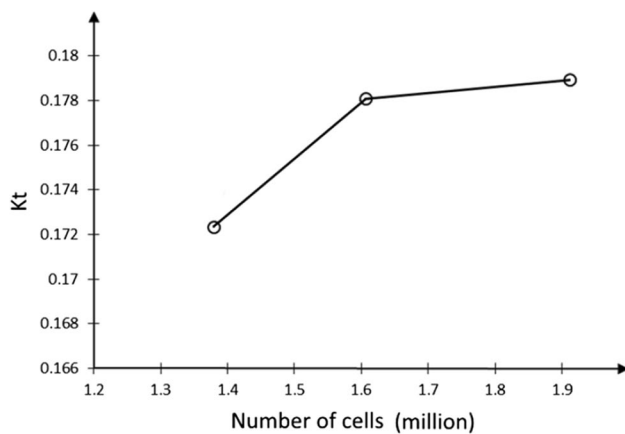


Fig. 7 The calculated values of thrust coefficient in different grids for $J=0.6$

Table 2 Calculations of discretization error for thrust coefficient of ducted propeller at $J=0.6$

Parameter	Value
N_1	1,911,436
N_2	1,606,484
N_3	1,378,872
r_{21}	1.05964
r_{32}	1.05225
K_{t1}	0.17891
K_{t2}	0.17807
K_{t3}	0.17233
p	38.74
$K_{\text{t ext}}^{21}$	0.17900
e_a^{21}	0.46%
e_{ext}^{21}	0.05%
GCI_{fine}	0.06%

$N_2=1,606,484$ and $N_3=1,378,872$. The grid refinement was done uniformly over the solution domain. The thrust coefficient (K_t), as an important integral variable in current simulation, was selected for grid convergence study. Figure 7 shows the calculated values of thrust coefficient in

different grids for advance coefficient of 0.6. The calculations of discretization error and numerical uncertainty are introduced in Table 2. In this Table N_1 , N_2 and N_3 are the total number of cells, in fine, medium and coarse grids, respectively. K_{t1} , K_{t2} and K_{t3} are calculated values of thrust coefficients for different grids. $r_{21} = (N_1/N_2)^{\frac{1}{3}}$ and $r_{32} = (N_2/N_3)^{\frac{1}{3}}$ are grid refinement factors. P is apparent order. $K_{\text{t ext}}^{21}$ is the extrapolated value of thrust coefficient. $e_a^{21} = |(K_{t1} - K_{t2})/K_{t1}|$ is approximate relative error. $e_{\text{ext}}^{21} = |(K_{\text{t ext}}^{21} - K_{t1})/K_{\text{t ext}}^{21}|$ is extrapolated relative error.

According to Table 2, the numerical uncertainty in fine-grid solution (the fine grid convergence index) is 0.06% for thrust coefficient of the ducted propeller.

3.3 Results of the ducted propeller

To ensure the iteration convergence, the iterations for each grid continue until the RSM of the residuals for each equation reduce to acceptable value of 10^{-4} , and the thrust force, as one of the main outputs, reaches a steady state. Table 3 represents a comparison between the results of complete domain, periodic domain and experimental results in the coarsest computational grid for an advance coefficient of 0.6. The values in Table 3 demonstrate that the assumption of periodic flow around the ducted propeller is reasonable, and, in addition to significant reduction in computational cost, can increase the accuracy in some cases.

In Fig. 8, the numerical results of hydrodynamic coefficients and efficiency are compared with experimental results in different advance coefficients, showing a good consistency between numerical and experimental results. Thrust coefficient of the ducted propeller is the summations of the duct thrust and propeller thrust. The thrust of the duct is increased and positive at low advance coefficient while it is decreased and negative at high advance coefficient. But thrust of the propeller is positive at all advance coefficients. Torque is only generated by the propeller. Also, computational errors of thrust and torque coefficients with respect to experimental data in different computational grids (coarse, medium and fine) are shown in Fig. 9. From

Table 3 Comparison between numerical and experimental results for both periodic and complete domains in $J=0.6$

Hydrodynamic coefficients	Numerical results for periodic domain	Numerical results for complete domain	Experimental results	Relative error for periodic domain (%)	Relative error for complete domain (%)
K_t	0.170322	0.160548	0.1884	9.01602	14.2370
K_q	0.0300973	0.028669	0.31066	3.09948	7.69666
$K_{t\text{prop}}$	0.1455023	0.13583	0.166858	11.8702	17.7286
K_{tn}	0.0248197	0.024718	0.021542	12.306	11.847
Efficiency	0.540399182	0.534759	0.5771	6.34329	7.32073

Fig. 8 Comparison between experimental and numerical results for the thrust coefficient (K_t), torque coefficient (K_q) and efficiency of ducted propeller in different advance coefficients

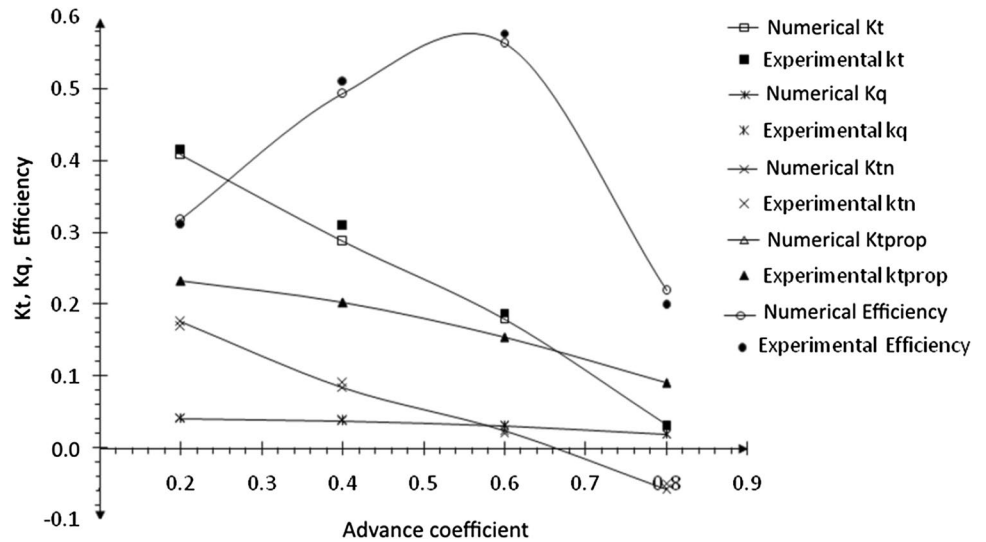
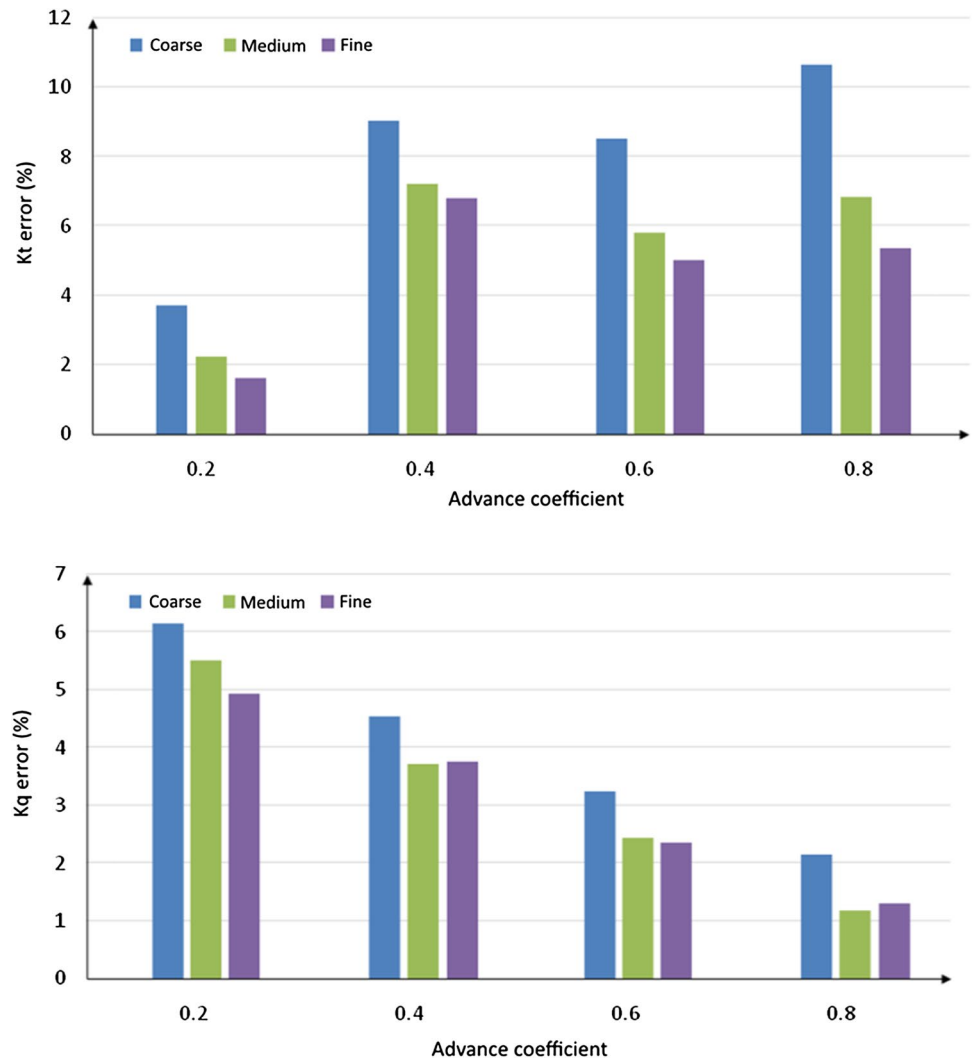


Fig. 9 Computational errors of thrust and torque coefficients with respect to experimental data in different computational grids



this figure, it can be seen that calculation error is reduced with the increasing number of grid cells. Also, in general, by increasing the advance coefficient, the calculation error of thrust coefficient is increased, while the calculation error of torque coefficient is decreased.

The pressure distributions on the ducted propeller for two advance coefficients of $J=0.4$ and $J=0.8$ are shown in Fig. 10. It is obvious that the propeller face is exposed

to a high pressure, while a low pressure occurs on the propeller back. The pressure difference between the face (pressure side) and the back (suction side) produce the propeller thrust. Also, the pressure distribution on duct shows a low pressure on internal face and a high pressure on external face of the duct.

Figure 10 Pressure distributions on the ducted propeller for two advance coefficients of $J=0.6$ and $J=0.8$.

Fig. 10 Pressure distributions on the ducted propeller for two advance coefficients of $J=0.6$ and $J=0.8$

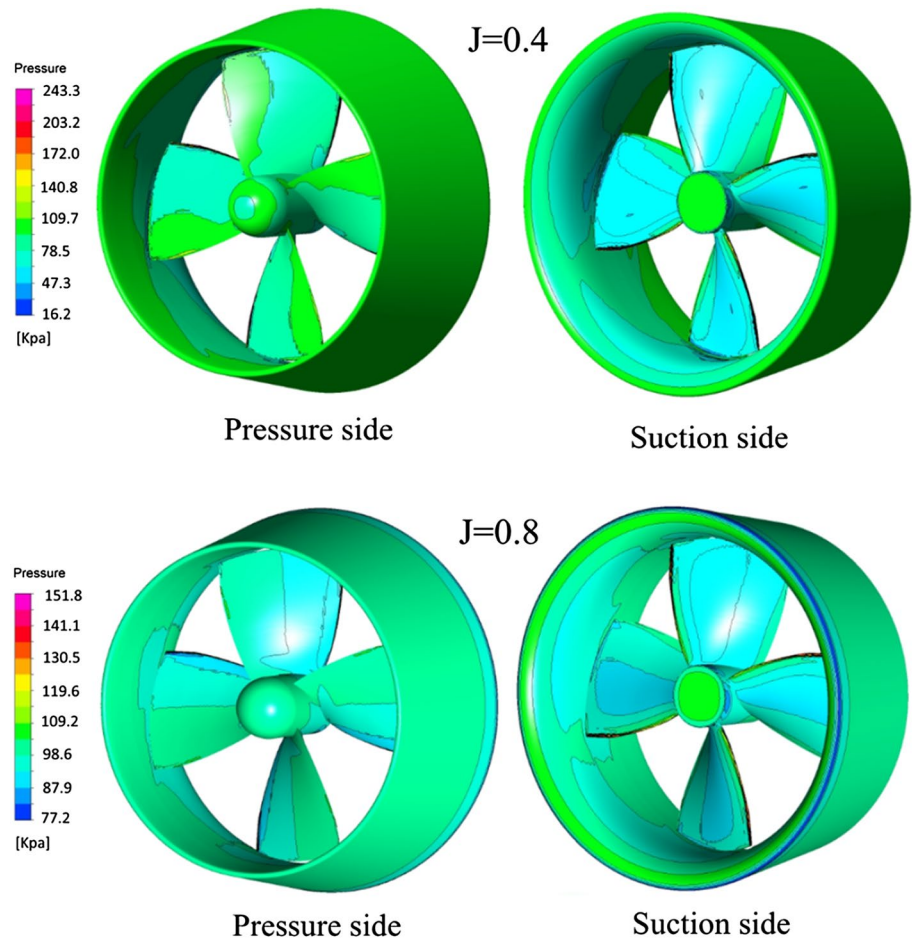
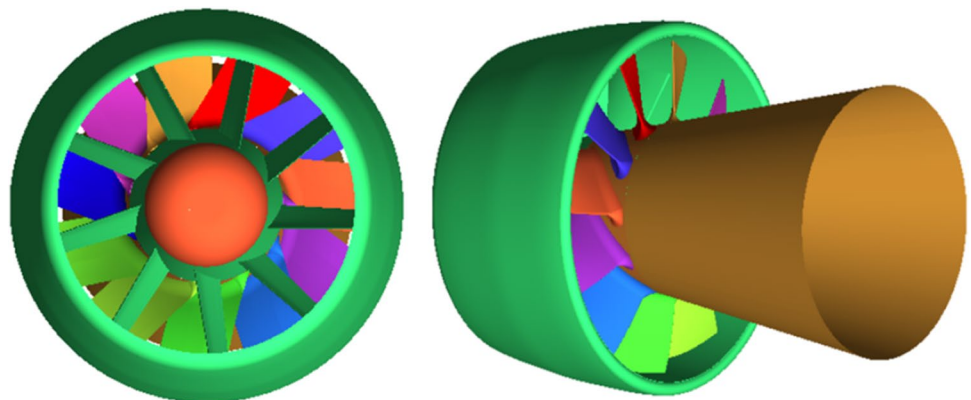


Fig. 11 3D model of pumpjet



4 Numerical analysis of pumpjet

Verification and validation study carried out in the previous section for the ducted propeller demonstrated that the presented numerical model can solve the flow around

Table 4 Main dimensions of pumpjet model

Parameter	Value
Number of rotor blades	11
Number of stator blades	9
Diameter of Rotor	404 mm
Diameter of Stator	378 mm
Fore radius of rotor hub	102 mm
Aft radius of the rotor hub	85 mm
Fore radius of the stator hub	85 mm
Aft radius of the stator hub	68.5 mm
Aft internal radius of duct	165 mm
Fore internal radius of duct	202.5 mm
Aft radius of inlet guide	102 mm
Fore radius of inlet guide	160.5 mm

a ducted propeller with high accuracy and convergency. According to the fact that a pumpjet is a ducted propeller with fixed blades located after the propeller, the governing equations, and boundary conditions can be considered as an appropriate mathematical model for analysis of flow around pumpjet. In addition, the computational grid type and commercial CFD solver used for the ducted propeller may also provide high order of convergence for analysis of pumpjet. Here, this model is implemented for a 3D model of the pumpjet as shown in Fig. 11. The main dimensions of the pumpjet are presented in Table 4.

Considering the interaction between rotor and stator in different rotation angles, the flow is naturally transient. So, to include the interaction effects, here the time-dependent solution with sliding mesh technique is used. Like the analysis of the ducted propeller in previous section, the flow around the rotor and stator is assumed periodic at any time and solving the flow is limited to only one blade of rotor and stator. The solution domain is divided into two periodic domains, one around the rotor blade with equations solved in moving reference frame and another around the stator blade with equations solved in stationary reference frame. Applied boundary conditions are the same as the ducted

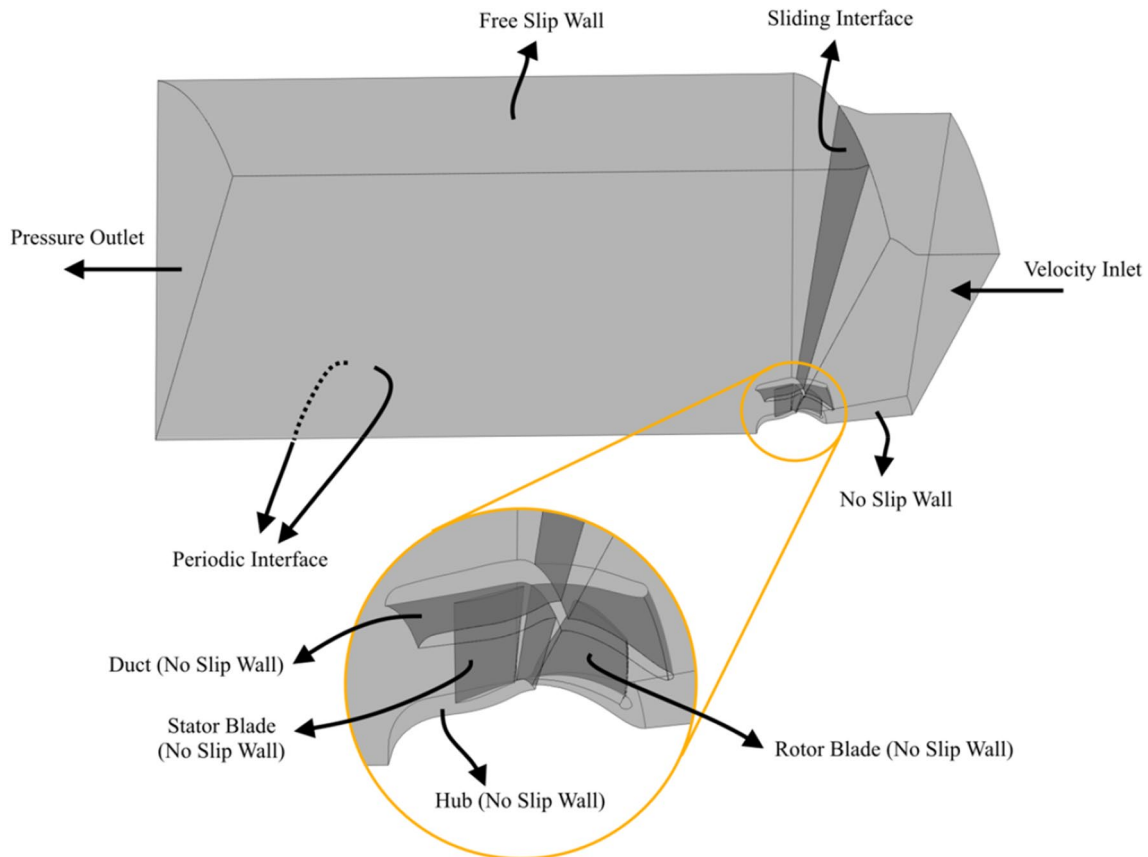
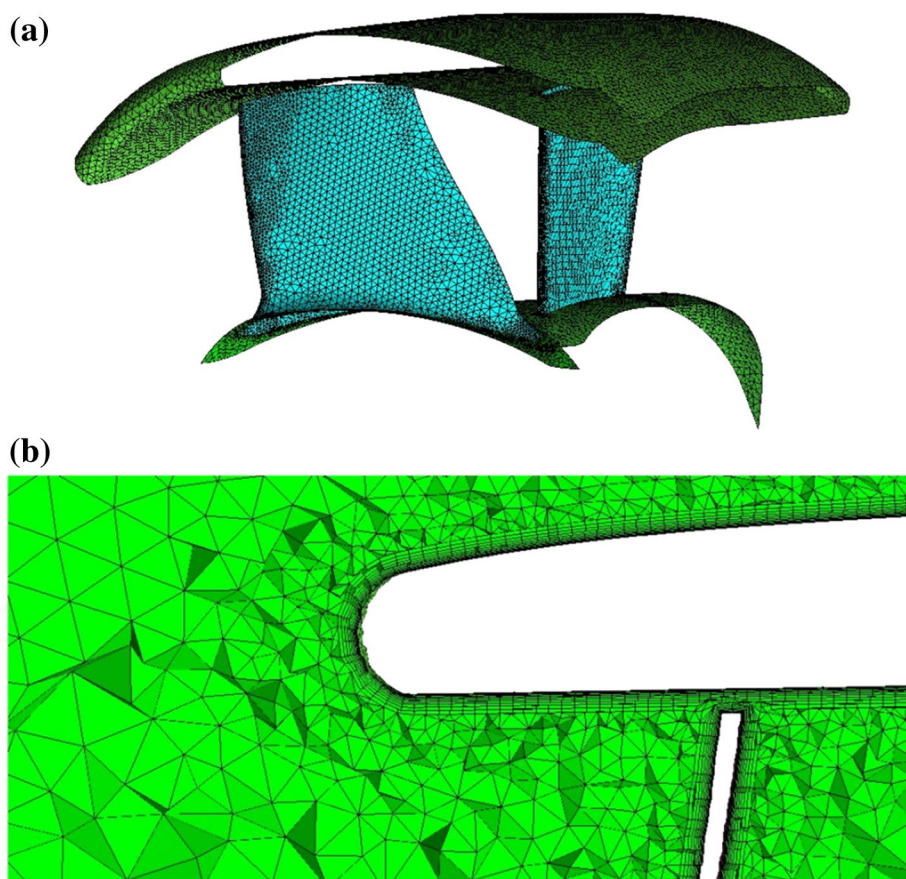


Fig. 12 Domains of rotor and stator and applied boundary conditions

Fig. 13 Schematic of the pumpjet computational grid, **a** on surface of rotor and stator, **b** inside the boundary layer of rotor tip and duct



propeller. The domains of rotor and stator with the applied boundary conditions are shown in Fig. 12.

The grid generation procedure for pumpjet is similar to the method used for ducted propeller in previous section. The grid is an unstructured mesh including tetrahedral cells with an inflation layer mesh inside the boundary layer flow. To study grid convergence, three different computational

grids were used. The size of the cells in the grids is almost the same size as the grid used for the ducted propeller. The surface mesh on stator, rotor, duct and hub are shown in Fig. 13. Also, in this figure, the inflation layer mesh inside the boundary layer of rotor tip and duct are presented (see Fig. 13c). The total number of cells in different grids is $N_1=6,450,426$, $N_2=5,367,522$ and $N_3=4,589,236$. Again, the total thrust coefficient was selected for grid convergence study. The calculations of discretization error at $J=1.95$ are presented in Table 5. The numerical uncertainty in fine-grid solution is 0.08% for total thrust coefficient of the pumpjet.

Table 5 Calculations of discretization error for total thrust coefficient of pumpjet at $J=1.95$

Parameter	Value
N_1	6,450,426
N_2	5,367,522
N_3	49,236
r_{21}	1.06317
r_{32}	1.05360
K_{t_1}	-0.05521
K_{t_2}	-0.05462
K_{t_3}	-0.04823
p	46.255
$K_{t_{ext}}^{21}$	-0.05525
e_a^{21}	1.06%
e_{ext}^{21}	0.07%
GCI_{fine}	0.08%

4.1 Results of pumpjet

Solving the transient flow around the pumpjet consists of two steps: first, a steady solution is calculated in a given situation of rotor relative to stator, as initial condition. Then, transient calculations are performed using the steady solution as initial solution. For each time step, iterations are continued until the RSM of the residuals for each governing equation is reduced to 10^{-4} and the hydrodynamic forces reach to a periodic mode in time. The period of hydrodynamic forces is equal to the duration between two same consecutive rotor–stator interactions (which depends on

Fig. 14 Convergence of thrust force

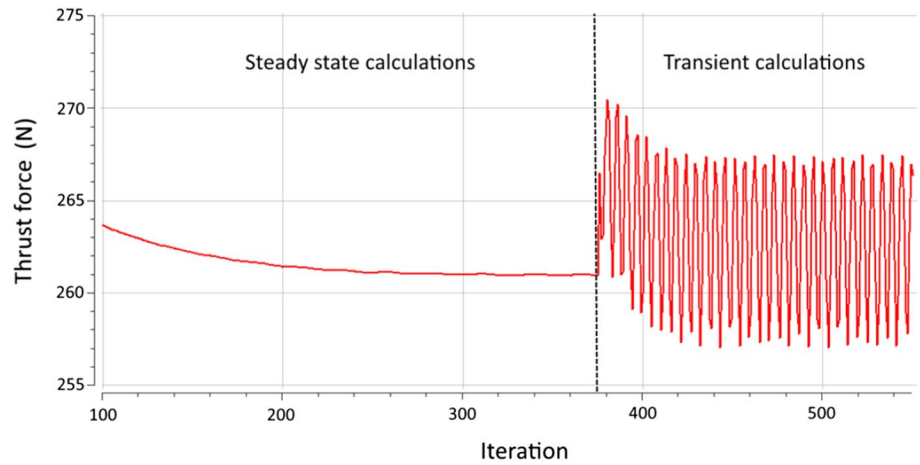
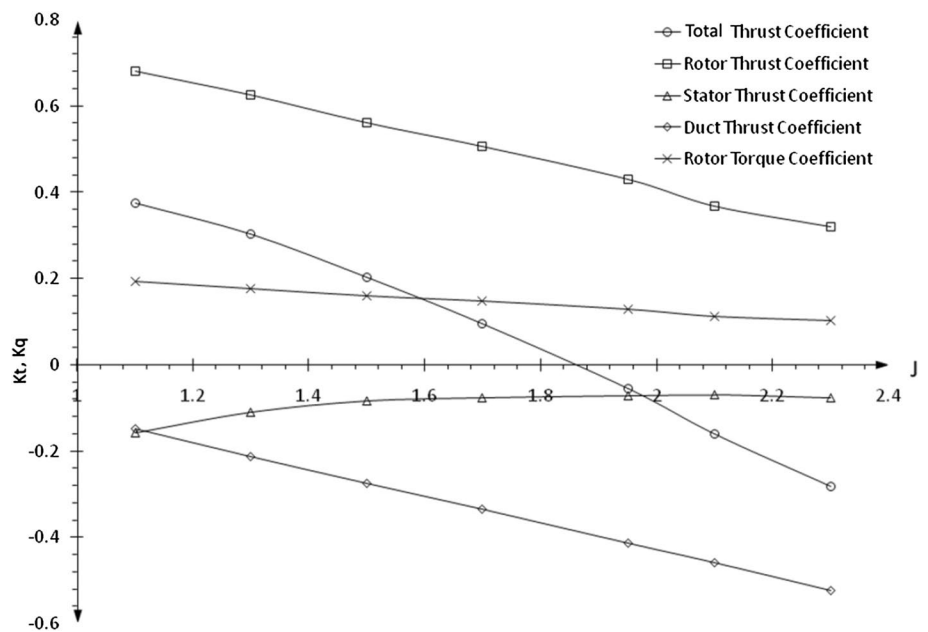


Table 6 Results of pumpjet numerical analysis

V_A (m/s)	n (RPM)	J	Rotor thrust coefficient	Stator thrust coefficient	Duct thrust coefficient	Total thrust coefficient	Rotor torque coefficient
5	681	1.1	0.68	-0.157	-0.147	0.375	0.192
7	808	1.3	0.62	-0.110	-0.212	0.302	0.177
9	900	1.5	0.56	-0.084	-0.274	0.201	0.159
11.3	1000	1.7	0.5	-0.075	-0.336	0.094	0.146
13	1000	1.95	0.43	-0.071	-0.414	-0.055	0.128
18	1286	2.1	0.36	-0.070	-0.459	-0.161	0.112
20.5	1342	2.3	0.31	-0.077	-0.523	-0.282	0.101

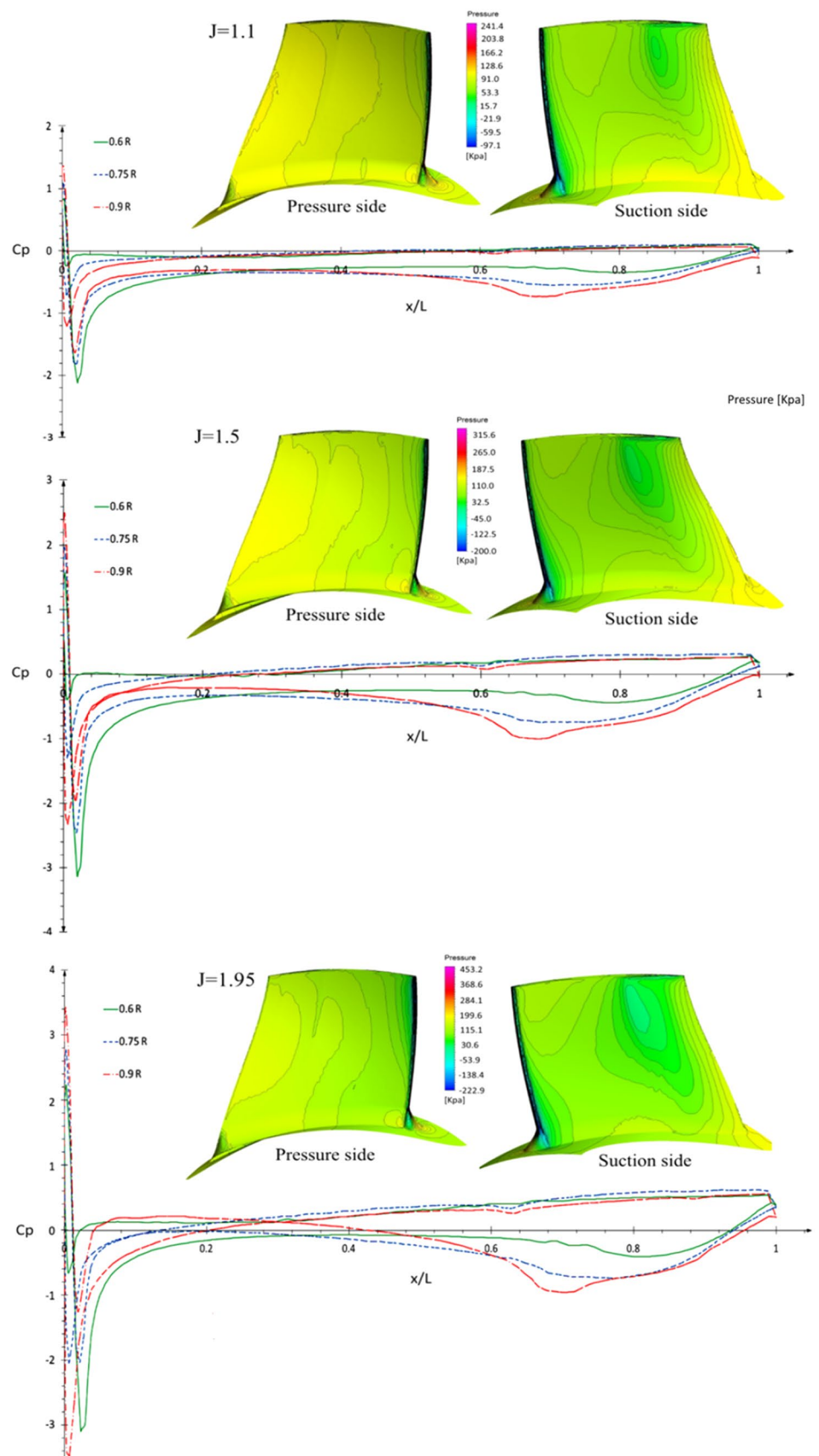
Fig. 15 Results of pumpjet numerical analysis in different advance coefficients (J)



the angular velocity of rotor). Figure 14 shows the convergence diagram of thrust force at $J = 1.95$. The convergence diagram has two parts. The first part illustrates the steady

state calculations and the second part shows the transient calculations, where the thrust reaches to a periodic mode resulted from periodic rotor- stator interactions.

Fig. 16 Pressure distributions on the suction and pressure sides of the rotor blade, with diagram of pressure coefficient along the chord at advance coefficient of 1.1, 1.5 and 1.95



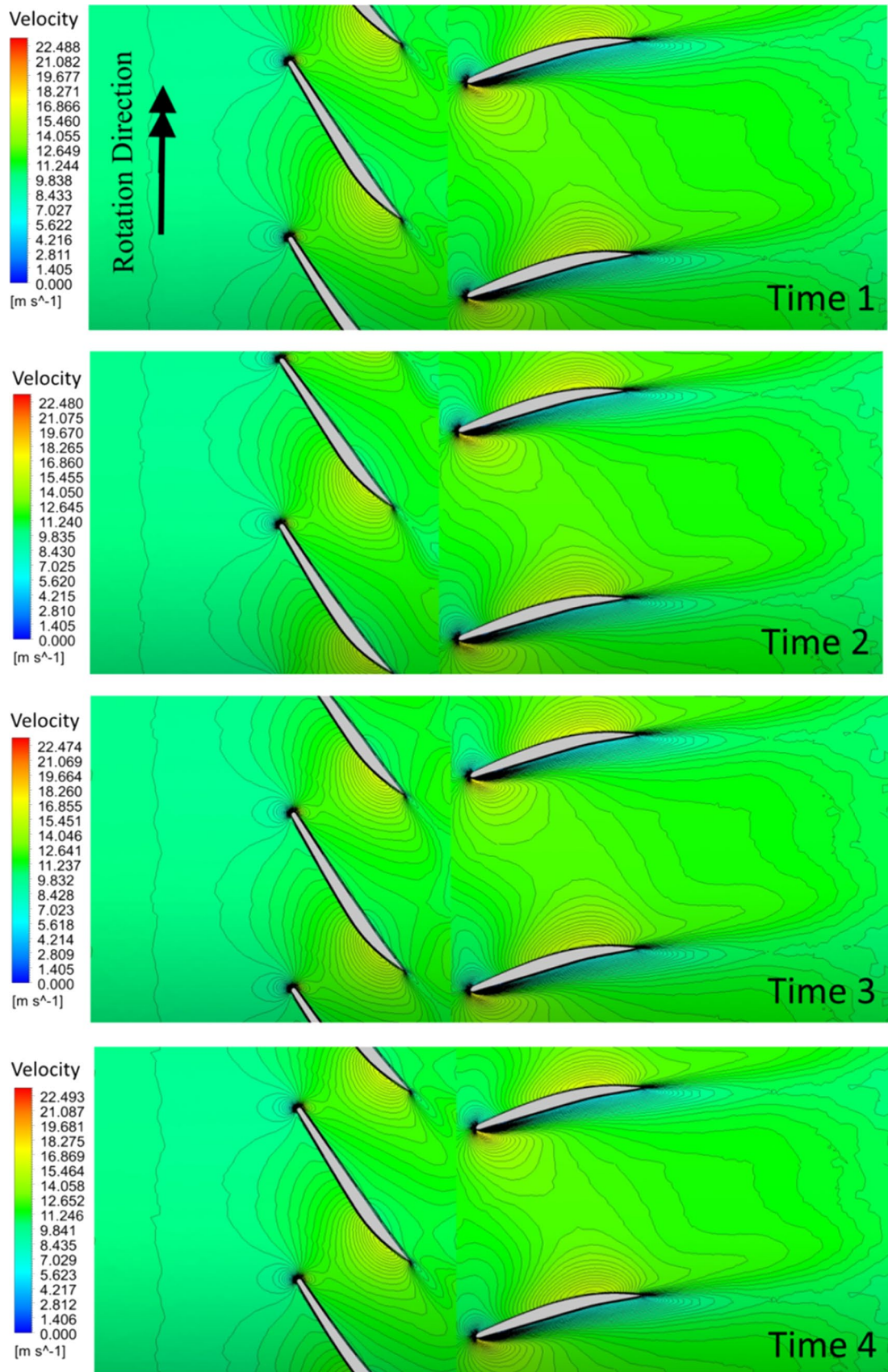


Fig. 17 Variations of velocity distribution for different rotor–stator interactions in a time period for advance coefficient of 1.95

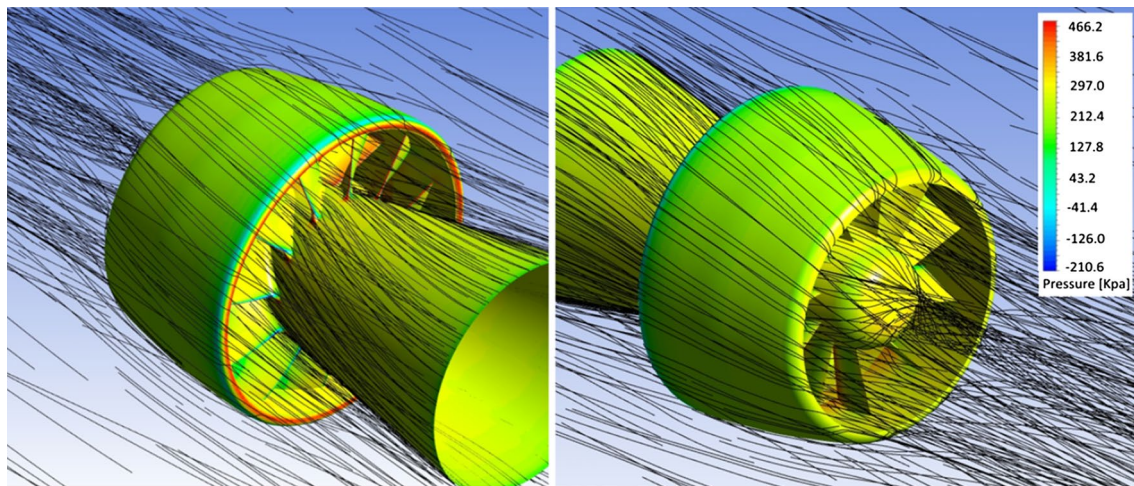


Fig. 18 Pressure distribution on pumpjet, with streamlines around pumpjet, at advance coefficient of 1.95

The time average values of thrust and torque coefficients at different advance coefficients are presented in Table 6. The related diagrams are also shown in Fig. 15. It can be seen that the total thrust coefficient is positive until $J=1.825$ and then it becomes negative. Although the stator leads to thrust reduction, it converts the outlet rotational flow of the rotor to an axial flow leading to increase of system efficiency.

The pressure distribution coefficient ($C_p = P/0.5\rho V_R^2$, where: $V_R^2 = V_A^2 + (2\pi rn)^2$) on the pressure and suction sides of the rotor blade for three different advance coefficients of 1.1, 1.5 and 1.95 are illustrated in Fig. 16. Furthermore, the graphs of pressure coefficient at different sections of 0.6R, 0.75R and 0.9R along the chord are presented in the same figure. As it is observed from the figure, the pressure difference between the suction and pressure sides of rotor blade is increased with increasing advance coefficient and the maximum pressure difference occurred at the maximum thickness of the blade. The variations of velocity distribution for different rotor–stator interactions in a time period for advance coefficient of 1.95 are shown in Fig. 17. Four consecutive time steps of the rotor and stator positions relative to each other are selected in a time period and shown in this figure. It can be seen that the velocity field around the blades change at deferent rotor positions in time. This leads to periodic fluctuations of thrust and torque forces (shown in Fig. 14). In Fig. 18, pressure distribution contour and including the streamlines around the pumpjet are illustrated at advance coefficient of 1.95 in two different views.

5 Conclusions

The finite volume numerical method was applied for analysis of the flow around a pumpjet propulsion system by solving the RANS equations with SST $k-\omega$ turbulent model. The presented numerical model was first applied to a ducted propeller and validated against the available experimental data. Those results of thrust, torque and efficiency for the ducted propeller are compared and shown to be in good agreement. Due to relatively good compatibility achieved between the numerical and experimental results, it can be concluded that the present model can be an appropriate model for solving the turbulent flow around a ducted propeller and a pumpjet. The assumption of periodic flow around the ducted propeller, in addition to significant reduction in computational cost, can increase the accuracy in some cases. In the analysis of the transient flow around the pumpjet, we concluded that the use of a steady solution as initial solution significantly improves the convergence speed. Authors' intend to work on the unsteady flow and the flow velocity inside the pumpjet as well as the duct shape, numbers of the stator and rotor blades are in the near future.

Acknowledgements The numerical results presented in this paper have been supported by the High Performance Computing Research Center (HPCRC) at Amirkabir University of Technology (AUT).

References

1. Carlton JS (2013) Marine propellers and propulsion, 3rd edn. Elsevier, Amsterdam

2. <http://www.gereports.com/post/74545156315/re-joyce-ge-to-launch-breakthrough-pumpjet-for>
3. Furuya, O., Chiang, W. L. (1988). A new pumpjet design theory. DTIC Report No. N00014-85-C-0050
4. Henderson RE, McMahon JF, Wislicenus GF (1964) A method for the design of pumpjets. ORL Report No. 63-0209-0-7
5. Zierke WC, Straka WA, Taylor PD (1993) An experimental investigation of the flow through an axial flow pump. *J Fluid Eng* 117(3):485–490
6. Hayden BJ (1994). Two-dimensional analysis of rotor suction and the impact on rotor-stator interaction noise. Master of Science Thesis, Dept. Aeronautics, Massachusetts Institute of Technology
7. Lee YT, Hah C, Loellbach J (1996) Flow analysis in a single-stage propulsion pump. *J Turbomach* 118(2):240–248
8. Ivanell S (2001). Hydrodynamic simulation of a torpedo with pumpjetpropulsion system. Master Thesis, Royal Institute of Technology, Stockholm, Sweden
9. Park WG, Jung YR, Kim CK (2005) Numerical flow analysis of single-stage ducted marine propulsor. *Ocean Eng* 32(10):1260–1277
10. Das HN, Jayakumar P, Saji VF, Yerram R (2006) CFD examination of interaction of flow on high speed submerged body with pumpjet propulsor. In: 5th International Conference on High Performance Marine vehicles, Australia, 8–10 Nov
11. Suryanarayana C, Satyanarayana B, Ramji K, Saiju A (2010) Experimental evaluation of pumpjet propulsor for an axisymmetric body in wind tunnel. *Int J Naval Archit Ocean Eng* 2:24–33
12. Suryanarayana C, Satyanarayana B, Ramji K (2010) Performance evaluation of an underwater body and pumpjet by model testing in cavitation tunnel. *Int J Naval Archit Ocean Eng* 2:57–67
13. Suryanarayana C, Satyanarayana B, Ramji K, Rao MN (2010) Cavitation studies on axi-symmetric underwater body with pumpjet propulsor in cavitation tunnel. *Int J Naval Archit Ocean Eng* 2:185–194
14. He L (2010) Numerical simulation of unsteady rotor/stator interaction and application to propeller/rudder combination. PhD thesis, Ocean Engineering Group, CAEE Department, University of Texas at Austin
15. Dong Y, Duan X, Feng S, Shao Z (2012) Numerical simulation of the overall flow field for underwater vehicle with pumpjet thruster. *Procedia Eng* 31:769–774
16. Rao ZQ, Li W, Yang CJ (2013) Simulation of unsteady interaction forces on a ducted propeller with pre-swirl stators. In: Third International Symposium on Marine Propulsors, smp'13, Launceston, Tasmania, Australia
17. Lu XJ, Zhou, Q.d., Fang B (2014) Hydrodynamic performance of distributed pumpjet propulsion system for underwater vehicle. *J Hydrodynam* 26:523–530
18. Ahn SJ, Kwon OJ (2015) Numerical investigation of a pumpjet with ring rotor using an unstructured mesh technique. *J Mech Sci Technol* 29:2897–2904
19. Huyer SA (2015). Postswirl maneuvering propulsor. *J Fluids Eng* 137(4):041104
20. Bontempo R, Cardone M, Manna M (2015) Performance analysis of ducted marine propellers. Part I—decelerating duct. *Appl Ocean Res* 58:322–330
21. Marko V, Roko D (2015) Neural network prediction of open water characteristics of ducted propeller. *J Marit Transp Sci* 49–50(1):101–115
22. Sun Y, Su YM, Wang X, Hu H (2016) Experimental and numerical analysis of the hydrodynamic performance of propeller boss cap fins in a propeller-rudder system. *Eng Appl Comput Fluid Mech* 10(1):145–159
23. Yu L, Greve M, Druckenbrod M, Abdel-Maksoud M (2013) Numerical analysis of ducted propeller performance under open water test condition. *J Mar Sci Technol* 18(3):381–394
24. Pana G, Lu L, Sahoo PK (2016) Numerical simulation of unsteady cavitating flows of pumpjet propulsor. *Ships Offshore Struct* 11(1):64–74
25. Oosterveld MWC (1973) Ducted propeller characteristics, Paper No. 4. In: Proceedings RINA Symposium on Ducted Propellers, Teddington, England
26. Raad PE, Celik IB, Ghia U, Roache PJ, Freitas CJ, Coleman H (2008). Procedure for estimation and reporting of uncertainty due to discretization in CFD applications. *J Fluids Eng Trans ASME*. doi:[10.1115/1.2960953](https://doi.org/10.1115/1.2960953)